Volume 9 No 2 December (2026)

e-ISSN: 2615-3270
p-ISSN: 2615-3599

Eigen Mathematics Journal

Homepage Journal: https://eigen.unram.ac.id/index.php/eigen

Mathematical Modelling of Coupled Wing–Engine Oscillations Using a Spring–Pendulum System

Billy Arifa Tengger[1*], Intrada Reviladi[1]

[1] *Department of Civil Engineering, Jenderal Soedirman University, Indonesia*
[*] *Corresponding author: billy.arifa@unsoed.ac.id*

ABSTRACT

Aircraft wings and underwing engine assemblies may experience oscillatory motion when the aircraft is subjected to disturbances such as turbulence or a hard landing. This study develops a reduced-order mathematical representation of the interaction by combining a vertical spring motion with a pendulum representing the engine. The generalized coordinates are the vertical wing displacement and the engine swing angle. Using Lagrange's equations, a system of two nonlinearly coupled second-order differential equations is obtained. The system has an equilibrium configuration at $(y^*, \theta^*) = (-mg/k, 0)$. After shifting the vertical coordinate to the equilibrium position and applying a first-order linearization, the system yields two uncoupled harmonic modes with natural angular frequencies $\omega_y = \sqrt{k/m}$ and $\omega_\theta = \sqrt{g/L}$. The corresponding frequencies in hertz are given by $f_y = \omega_y/(2\pi)$ and $f_\theta = \omega_\theta/(2\pi)$. For the illustrative parameters $m = 1000$ kg, $k = 20{,}000$ N/m, and $L = 2$ m, the corresponding natural frequencies are approximately 0.712 Hz and 0.352 Hz. The nonlinear system is numerically integrated using the DOP853 method. For the initial conditions $x(0) = 0.05$ m, $\dot{x}(0) = 0$, $\theta(0) = 5°$, and $\dot{\theta}(0) = 0$, simulations for $k = 15{,}000$, $20{,}000$, and $25{,}000$ N/m produce responses that remain bounded over the simulated intervals. Over the 10-s stiffness-comparison interval, the maximum absolute shifted vertical displacement decreases from 0.0757 m to 0.0500 m, while the maximum angular response reaches 5.795° at $k = 25{,}000$ N/m. The numerically estimated frequencies differ from the analytical predictions by no more than 3.37%. Energy-conservation and solver-sensitivity checks further indicate numerical consistency under the tested computational settings. The model excludes aerodynamic loading, structural damping, and external excitation and is intended as a reduced-order mathematical representation rather than a predictor of actual aircraft behavior.

Keywords: Wing–Engine oscillation, Spring–Pendulum model, Nonlinear coupling, Local linearization, Spring-Stiffness sensitivity

Received : 08-09-2026;
Revised : 01-11-2026;
Accepted : 17-11-2026;
Published : 25-11-2026;

DOI: https://doi.org/10.29303/emj.v9i2.485

This work is licensed under a CC BY-NC-SA 4.0 International license

1. Introduction

Aircraft structures experience dynamic loading throughout operation due to aerodynamic disturbances, turbulence, landing impacts, and transient excitation. These loads may induce vibration in flexible components, particularly in wing structures and attached components such as pylons and

external masses. Previous investigations have shown that under-wing store mass and engine-related excitation can influence the vibration and aeroelastic responses of wing structures [1, 2]. Therefore, understanding the interaction between flexible wing motion and attached components remains an important topic in structural dynamics and aeroelasticity [3–9].

Experimental and theoretical studies of aircraft structures have demonstrated that elastic deformation modes can affect the dynamic behavior of aerospace systems [10]. However, a complete wing–pylon–engine model generally requires consideration of distributed structural properties, aerodynamic forces, damping mechanisms, and multiple degrees of freedom. Although high-fidelity models provide more detailed predictions, their complexity may limit the analysis of fundamental dynamic interactions. For this reason, reduced-order models are frequently used in vibration studies to capture dominant physical mechanisms while maintaining mathematical tractability [11–13]. Recent developments in nonlinear aeroelastic reduction also demonstrate how reduced-order descriptions can retain selected nonlinear effects while reducing model complexity [7, 13].

The mechanical representation of the wing–engine configuration requires a model that accounts for both vertical translation and angular motion. A spring–pendulum system provides a suitable reduced-order framework for this purpose, in which the vertical flexibility of the wing support is represented by a linear spring, while the engine motion is described by a point mass connected through a rigid link. Since the engine position depends on both the vertical displacement of the support and the pendulum angle, its kinetic energy contains a mixed term involving the vertical and angular velocities. This term gives rise to nonlinear coupling in the resulting equations of motion. The Lagrangian formulation provides a systematic approach to deriving these coupled equations from the kinetic and potential energies of the system [14–17].

Previous studies on pendulum-based vibration absorbers have investigated various mechanical configurations and nonlinear response mechanisms. Kecik [18] proposed an autoparametric pendulum vibration absorber combined with an energy-harvesting mechanism, focusing on simultaneous vibration mitigation and energy recovery. Abundis-Fong et al. [19] investigated a nonlinear cantilever-beam absorber coupled to a resonantly excited oscillator, using the method of multiple scales to analyze the system response and determine absorber parameters. Amer et al. [20] studied a pendulum attached to a tuned absorber under harmonic excitation, examining primary and internal resonance conditions through the Lagrangian formulation and the method of multiple scales. Hurel et al. [21] investigated nonlinear vibratory energy exchanges between a two-degree-of-freedom pendulum and a nonlinear absorber, while Hurel [22] further considered nonlinear absorber design and experimental validation for a two-degree-of-freedom pendulum. Amer et al. [23] subsequently examined a two-degree-of-freedom tuned-absorber system involving a pendulum whose pivot follows a prescribed Lissajous trajectory under harmonic excitation. More recently, Zhang et al. [24] investigated large-amplitude oscillations of a pendulum absorber-harvester with a nonlinear spring, including its bifurcation and chaotic responses.

These studies demonstrate the importance of nonlinear coupling, resonance, and parameter selection in pendulum-based vibration systems. However, their primary objectives concern vibration mitigation, resonance behavior, or energy harvesting rather than the mathematical representation of an underwing engine moving relative to a vertically flexible wing support.

Although previous studies have extensively examined pendulum-based vibration absorbers and aircraft structural vibration, these research directions generally address different modelling objectives. Aircraft vibration studies often consider structural deformation, aerodynamic effects, and complex wing–pylon configurations, whereas pendulum-based studies primarily focus on absorber performance, resonance, and energy harvesting. The relationship between these two perspectives motivates the use

of a simplified mechanical representation that directly connects the vertical flexibility of a wing support with the angular motion of an underwing engine.

Accordingly, this study considers an idealized wing–engine configuration in which the vertical flexibility of the wing is represented by an equivalent linear spring and the engine is modeled as a point mass suspended through a rigid link. The proposed model is not intended to reproduce the complete aeroelastic response of an aircraft. Instead, it provides a low-order mathematical framework for examining the nonlinear interaction between vertical wing displacement and engine angular oscillation, together with their local linear behavior near the equilibrium configuration.

The main contribution of this study is the mathematical characterization of a simplified spring–pendulum representation of wing–engine interaction. The formulation establishes the coupled nonlinear equations governing the vertical and angular motions of the system. The equilibrium and local linear analyses further show that, although the original equations are nonlinearly coupled, the first-order approximation yields two independent oscillatory modes with natural frequencies determined by the spring-to-mass and gravity-to-length ratios. Furthermore, the numerical investigation quantifies the effects of spring stiffness on the vertical and angular responses and compares the numerically estimated frequencies with their analytical small-oscillation predictions. These results clarify the mathematical characteristics and limitations of the proposed reduced-order model.

2. Mathematical Model Formulation

2.1. Model assumptions and variables

The physical motivation of the proposed model and its equivalent mechanical representation are illustrated in Figure 1. The aircraft configuration shown in Figure 1(a) represents the interaction between vertical wing motion and engine oscillation. Based on this physical interpretation, the wing flexibility and engine motion are simplified into an equivalent spring–pendulum system, as shown in Figure 1(b).

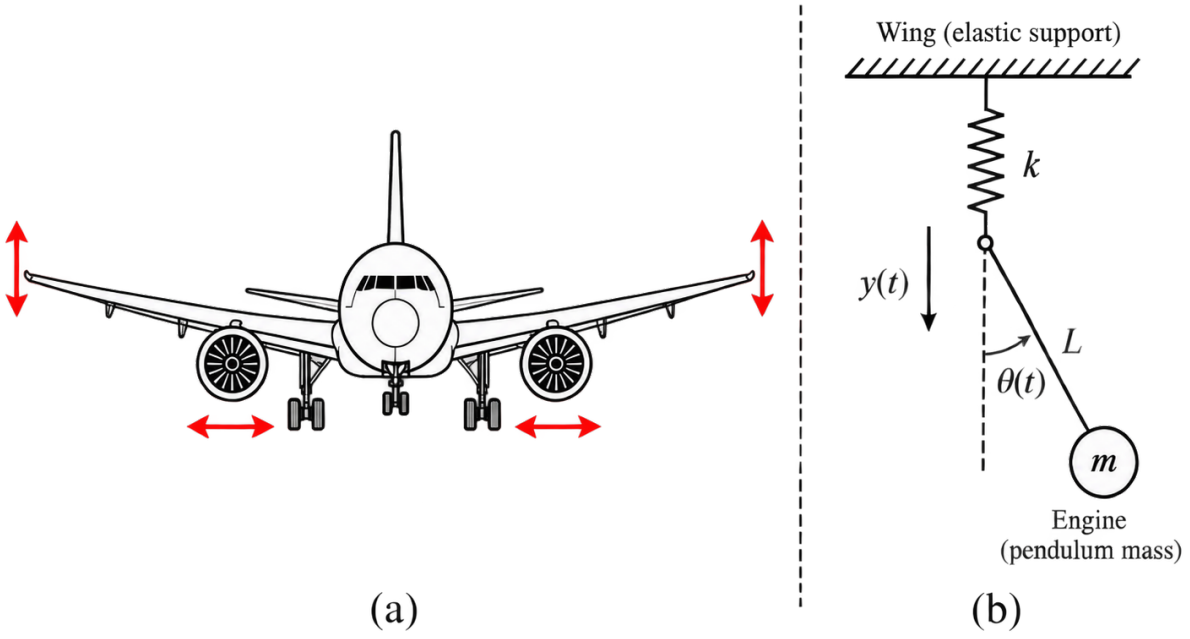

Figure 1. Physical motivation and simplified mechanical representation of the coupled wing–engine oscillation system.

The following assumptions are used:

1. the wing motion is represented only in the vertical direction;
2. the equivalent wing flexibility is represented by a linear spring of stiffness k;
3. the engine is represented by a point mass m connected to the wing by a rigid support of length L;
4. the engine swings in a vertical plane with angle $\theta(t)$;
5. aerodynamic drag and structural damping are neglected;
6. gravitational acceleration g is constant.

The vertical coordinate of the wing is denoted by $y(t)$. If (X, Y) denotes the engine position, then the geometry gives

$$X = L\sin\theta, \qquad Y = y - L\cos\theta. \tag{1}$$

The variables and parameters used in the model are summarized in Table 1.

Table 1. Variables and parameters of the model.

Symbol	Description	Unit
$y(t)$	vertical coordinate of the wing support	m
$\theta(t)$	swing angle of the engine	rad
m	equivalent engine mass	kg
k	equivalent vertical spring stiffness	N/m
L	engine support length	m
g	gravitational acceleration	m/s^2

2.2. Kinetic and potential energy

Differentiating Equation (1) with respect to time gives

$$\dot{X} = L\dot{\theta}\cos\theta, \qquad \dot{Y} = \dot{y} + L\dot{\theta}\sin\theta. \tag{2}$$

Hence, the square of the engine velocity is

$$\begin{aligned} V_m^2 &= \dot{X}^2 + \dot{Y}^2 \\ &= \dot{y}^2 + L^2\dot{\theta}^2 + 2L\dot{y}\dot{\theta}\sin\theta. \end{aligned} \tag{3}$$

The kinetic energy is therefore

$$E_k = \frac{1}{2}m\left(\dot{y}^2 + L^2\dot{\theta}^2 + 2L\dot{y}\dot{\theta}\sin\theta\right). \tag{4}$$

The potential energy consists of the gravitational and spring components,

$$E_p = mg(y - L\cos\theta) + \frac{1}{2}ky^2. \tag{5}$$

The total mechanical energy of the system is defined as the sum of the kinetic and potential energies, $E = E_k + E_p$. In the Lagrangian formulation, however, the Lagrangian is defined as the difference between these two energies, $\mathcal{L} = E_k - E_p$. This formulation is adopted because the equations of motion for a conservative mechanical system can be systematically derived through the Euler–Lagrange equations expressed in generalized coordinates. Substituting the kinetic and potential energies given in Equations (4) and (5), respectively, into the Lagrangian definition yields

$$\mathcal{L} = \frac{1}{2}m\left(\dot{y}^2 + L^2\dot{\theta}^2 + 2L\dot{y}\dot{\theta}\sin\theta\right) - \frac{1}{2}ky^2 - mg(y - L\cos\theta). \tag{6}$$

2.3. Governing equations

The equations of motion are derived by applying the Euler–Lagrange equation to each generalized coordinate $q \in \{y, \theta\}$:

$$\frac{d}{dt}\left(\frac{\partial \mathcal{L}}{\partial \dot{q}}\right) - \frac{\partial \mathcal{L}}{\partial q} = 0.$$

For the angular coordinate θ, the required partial derivatives are

$$\begin{aligned}
\frac{\partial \mathcal{L}}{\partial \dot{\theta}} &= mL^2\dot{\theta} + mL\dot{y}\sin\theta, \\
\frac{d}{dt}\left(\frac{\partial \mathcal{L}}{\partial \dot{\theta}}\right) &= mL^2\ddot{\theta} + mL\ddot{y}\sin\theta + mL\dot{y}\dot{\theta}\cos\theta, \\
\frac{\partial \mathcal{L}}{\partial \theta} &= mL\dot{y}\dot{\theta}\cos\theta - mgL\sin\theta.
\end{aligned}$$

Substituting these expressions into the Euler–Lagrange equation gives

$$mL^2\ddot{\theta} + mL\ddot{y}\sin\theta + mL\dot{y}\dot{\theta}\cos\theta - mL\dot{y}\dot{\theta}\cos\theta + mgL\sin\theta = 0.$$

After cancellation of the mixed-velocity terms and division by mL, the equation of motion for θ becomes

$$L\ddot{\theta} + \ddot{y}\sin\theta = -g\sin\theta. \tag{7}$$

Similarly, for the vertical coordinate y, the partial derivatives are

$$\begin{aligned}
\frac{\partial \mathcal{L}}{\partial \dot{y}} &= m\dot{y} + mL\dot{\theta}\sin\theta, \\
\frac{d}{dt}\left(\frac{\partial \mathcal{L}}{\partial \dot{y}}\right) &= m\ddot{y} + mL\ddot{\theta}\sin\theta + mL\dot{\theta}^2\cos\theta, \\
\frac{\partial \mathcal{L}}{\partial y} &= -ky - mg.
\end{aligned}$$

Substituting these expressions into the Euler–Lagrange equation yields

$$m\ddot{y} + mL\ddot{\theta}\sin\theta + mL\dot{\theta}^2\cos\theta + ky + mg = 0.$$

Dividing by m and rearranging the terms, the equation of motion for y is obtained as

$$L\ddot{\theta}\sin\theta + \ddot{y} = -L\dot{\theta}^2\cos\theta - \frac{k}{m}y - g. \tag{8}$$

To obtain an explicit expression for the vertical acceleration, $\ddot{y}$, we first eliminate $\ddot{\theta}$ from Equations (7) and (8). Rearranging Equation (7) gives

$$\ddot{\theta} = -\frac{\sin\theta}{L}(\ddot{y} + g).$$

Substituting this expression into Equation (8) and collecting the terms involving $\ddot{y}$, we obtain

$$\ddot{y}(1 - \sin^2\theta) = -L\dot{\theta}^2\cos\theta - \frac{k}{m}y - g(1 - \sin^2\theta).$$

Using the trigonometric identity $1 - \sin^2\theta = \cos^2\theta$, the above equation can be written as

$$\ddot{y} = -\frac{1}{\cos^2\theta}\left(L\dot{\theta}^2\cos\theta + \frac{k}{m}y + g\cos^2\theta\right). \tag{9}$$

The angular acceleration, $\ddot{\theta}$, can then be obtained by substituting Equation (9) into Equation (7). In particular, Equation (9) gives

$$\begin{aligned}\ddot{y} + g &= -\frac{L\dot{\theta}^2\cos\theta + \frac{k}{m}y + g\cos^2\theta}{\cos^2\theta} + g \\ &= -\frac{L\dot{\theta}^2\cos\theta + \frac{k}{m}y}{\cos^2\theta}.\end{aligned}$$

Substituting this result into Equation (7) yields

$$\begin{aligned}\ddot{\theta} &= \frac{\sin\theta}{L\cos^2\theta}\left(L\dot{\theta}^2\cos\theta + \frac{k}{m}y\right) \\ &= \dot{\theta}^2\tan\theta + \frac{ky\tan\theta}{mL\cos\theta}.\end{aligned}$$

Thus, the angular acceleration is expressed as

$$\ddot{\theta} = \dot{\theta}^2\tan\theta + \frac{ky\tan\theta}{mL\cos\theta}. \tag{10}$$

The above elimination involves division by $\cos^2\theta$. Therefore, the explicit acceleration expressions in Equations (9) and (10) are valid for $\cos\theta \neq 0$. This condition is satisfied in a neighborhood of the downward-hanging equilibrium, $\theta = 0$, considered in this study. To verify the consistency of the derived expressions, Equations (9) and (10) are substituted back into the original Equations (7) and (8). For Equation (7), this substitution gives

$$\begin{aligned}L\ddot{\theta} + \ddot{y}\sin\theta &= \frac{L\dot{\theta}^2\sin\theta}{\cos\theta} + \frac{ky\sin\theta}{m\cos^2\theta} - \frac{L\dot{\theta}^2\sin\theta}{\cos\theta} - \frac{ky\sin\theta}{m\cos^2\theta} - g\sin\theta \\ &= -g\sin\theta.\end{aligned}$$

Similarly, substituting Equations (9) and (10) into the left-hand side of Equation (8) gives

$$\begin{aligned}L\ddot{\theta}\sin\theta + \ddot{y} &= L\left(\dot{\theta}^2\tan\theta + \frac{ky\tan\theta}{mL\cos\theta}\right)\sin\theta - \frac{1}{\cos^2\theta}\left(L\dot{\theta}^2\cos\theta + \frac{k}{m}y + g\cos^2\theta\right) \\ &= \frac{L\dot{\theta}^2}{\cos\theta}(\sin^2\theta - 1) + \frac{ky}{m\cos^2\theta}(\sin^2\theta - 1) - g \\ &= -L\dot{\theta}^2\cos\theta - \frac{k}{m}y - g.\end{aligned}$$

This result is identical to the right-hand side of Equation (8). Therefore, both original equations of motion are satisfied by the derived acceleration expressions.

The wing–engine system is dynamically coupled because the equations of motion for the two generalized coordinates are not independent. In Equations (7) and (8), the vertical acceleration $\ddot{y}$ and the angular acceleration $\ddot{\theta}$ appear together in both equations. The origin of this coupling can be traced to the mixed term $mL\dot{y}\dot{\theta}\sin\theta$ in the kinetic energy expression in Equation (4). Consequently, the vertical and angular accelerations must be determined simultaneously from the equations of motion, reflecting the dynamical interaction between the wing support and the engine.

3. Equilibrium and Local Linear Analysis

An equilibrium occurs when

$$\dot{y} = \dot{\theta} = \ddot{y} = \ddot{\theta} = 0.$$

From Equations (9)–(10), a physically relevant equilibrium is

$$(y^*, \theta^*) = \left(-\frac{mg}{k}, 0\right). \tag{11}$$

The nonzero value of y^* represents the static spring displacement caused by gravity according to the sign convention used in the model.

For convenience, define the vertical displacement relative to the static equilibrium by

$$x = y + \frac{mg}{k}. \tag{12}$$

Therefore, $x = 0$ at equilibrium. Since the angular equilibrium considered is $\theta^* = 0$, the equilibrium position in the transformed coordinates becomes $(x^*, \theta^*) = (0, 0)$, with $\dot{x}^* = \dot{\theta}^* = 0$. Substituting Equation (12) into the nonlinear model gives

$$\ddot{x} = -\frac{1}{\cos^2\theta}\left(L\dot{\theta}^2\cos\theta + \frac{k}{m}x - g\sin^2\theta\right), \tag{13}$$

and

$$\ddot{\theta} = \dot{\theta}^2\tan\theta + \left(\frac{k}{m}x - g\right)\frac{\tan\theta}{L\cos\theta}. \tag{14}$$

In the present analysis, a neighborhood of the equilibrium refers to a region in the state space where the vertical displacement, vertical velocity, angular displacement, and angular velocity are all sufficiently close to their equilibrium values. In terms of the state variables, this means that $(x, \dot{x}, \theta, \dot{\theta})$ is close to $(0, 0, 0, 0)$. No specific numerical radius is prescribed for this neighborhood; it represents the local region in which the behavior of the system is examined through linearization. Consequently, the linearized model describes the local dynamics near the equilibrium and should not be interpreted as a representation of the nonlinear system for arbitrary initial conditions.

Within this neighborhood, the small-angle approximation is introduced by assuming that the angular displacement satisfies $|\theta| \ll 1$ rad. Accordingly, the trigonometric functions are approximated about $\theta = 0$ as $\sin\theta \approx \theta$, $\cos\theta \approx 1$, and $\tan\theta \approx \theta$. By retaining only first-order terms in the perturbation variables, higher-order terms involving $\dot{\theta}^2$, $\sin^2\theta$, and $x\tan\theta$ are neglected because they represent second-order or higher contributions. The resulting local linear system becomes

$$\ddot{x} + \frac{k}{m}x = 0, \qquad \ddot{\theta} + \frac{g}{L}\theta = 0. \tag{15}$$

The resulting linearized equations describe two independent harmonic oscillators. Although the original nonlinear equations contain coupling between the vertical and angular motions, these coupling

terms vanish in the first-order approximation because they are of second or higher order. Nevertheless, the nonlinear coupling remains present in the original system and may influence the response at finite oscillation amplitudes. The corresponding natural angular frequencies of the vertical and angular motions, respectively, are

$$\omega_y = \sqrt{\frac{k}{m}}, \qquad \omega_\theta = \sqrt{\frac{g}{L}}. \tag{16}$$

To examine the stability characteristics of the linearized system, Equations (15) are first expressed as a system of four first-order differential equations. Define the state variables as

$$z_1 = x, \qquad z_2 = \dot{x}, \qquad z_3 = \theta, \qquad z_4 = \dot{\theta}.$$

The corresponding state vector is

$$\mathbf{z} = \begin{bmatrix} z_1 & z_2 & z_3 & z_4 \end{bmatrix}^T.$$

Using the linearized equations in Equation (15), the time derivatives of the state variables are

$$\begin{aligned} \dot{z}_1 &= z_2, \\ \dot{z}_2 &= -\frac{k}{m} z_1, \\ \dot{z}_3 &= z_4, \\ \dot{z}_4 &= -\frac{g}{L} z_3. \end{aligned}$$

Thus, the system can be written in state-space form as $\dot{\mathbf{z}} = A\mathbf{z}$, where

$$A = \begin{bmatrix} 0 & 1 & 0 & 0 \\ -\frac{k}{m} & 0 & 0 & 0 \\ 0 & 0 & 0 & 1 \\ 0 & 0 & -\frac{g}{L} & 0 \end{bmatrix}.$$

The characteristic equation is obtained from $\det(\lambda I - A) = 0$, which gives

$$\left(\lambda^2 + \frac{k}{m}\right)\left(\lambda^2 + \frac{g}{L}\right) = 0.$$

The eigenvalues of the state matrix A are

$$\lambda_{1,2} = \pm i\sqrt{\frac{k}{m}}, \qquad \lambda_{3,4} = \pm i\sqrt{\frac{g}{L}}. \tag{17}$$

All eigenvalues are purely imaginary. Therefore, the linearized undamped system exhibits neutral stability, rather than asymptotic stability [17]. This behavior is consistent with the absence of damping and other dissipative mechanisms in the model. Consequently, the oscillations of the linearized system persist without decaying amplitudes.

4. Numerical Simulation

4.1. Parameter values and computational procedure

The nonlinear system in Equations (13)–(14) was solved numerically as an initial-value problem using the `solve_ivp` routine provided by the SciPy numerical computing environment [25]. The time integration employed the DOP853 method, an explicit Runge-Kutta method of order eight [26].

The numerical integration was performed with a relative tolerance of 10^{-10}, an absolute tolerance of 10^{-12}, and a maximum integration step size of 0.01 s. For plotting and response analysis, the numerical solutions were evaluated at uniformly spaced output times with an interval of 0.001 s. The adaptive solver step size was controlled separately by the maximum step size specified above.

The parameter values presented in Table 2 are prescribed for an illustrative numerical investigation rather than obtained from measurements of a specific aircraft configuration. Since the present study considers an idealized mechanical representation, the equivalent engine mass $m = 1000$ kg and support length $L = 2.0$ m are adopted as model parameters and should not be interpreted as measured characteristics of an actual aircraft. The baseline spring stiffness is set to $k = 20{,}000$ N/m to establish the reference numerical configuration. With these values, the local linear analysis gives vertical and angular natural frequencies of approximately 0.712 Hz and 0.352 Hz, respectively. These parameter values establish a reference configuration with distinct vertical and angular oscillation time scales, allowing the corresponding responses and their nonlinear interaction to be examined numerically. The gravitational acceleration is taken as $g = 9.81$ m/s^2, which is the rounded value of the standard acceleration of gravity of 9.80665 m/s^2 reported by NIST [27].

The initial conditions are prescribed as initial perturbations from the static equilibrium, with $x(0) = 0.05$ m and $\theta(0) = \pi/36$ rad (5°). The initial velocities are set to zero, representing release from rest at the prescribed initial displacements. These initial conditions are selected for numerical illustration and are not obtained from measured aircraft disturbances. Angular quantities are expressed in radians throughout the numerical implementation.

Table 2. Illustrative parameter values and initial conditions.

Parameter	Value	Unit
m	1000	kg
L	2.0	m
k	20,000	N/m
g	9.81	m/s^2
$x(0)$	0.05	m
$\dot{x}(0)$	0	m/s
$\theta(0)$	$\pi/36$	rad
$\dot{\theta}(0)$	0	rad/s

Using the baseline parameter values in Table 2, the analytical natural frequencies obtained from Equation (16) are

$$f_y^{\mathrm{lin}} = \frac{1}{2\pi}\sqrt{\frac{k}{m}} \approx 0.712 \text{ Hz}, \qquad f_\theta^{\mathrm{lin}} = \frac{1}{2\pi}\sqrt{\frac{g}{L}} \approx 0.352 \text{ Hz}.$$

4.2. Vertical and angular response

The baseline numerical responses were evaluated over the time interval $0 \le t \le 20$ s. Figure 2 shows the vertical displacement relative to static equilibrium. The displacement remains bounded during the 20-s simulation and oscillates approximately within −0.0529 m and 0.0530 m. The waveform is not perfectly sinusoidal because the original nonlinear terms are retained in the numerical model.

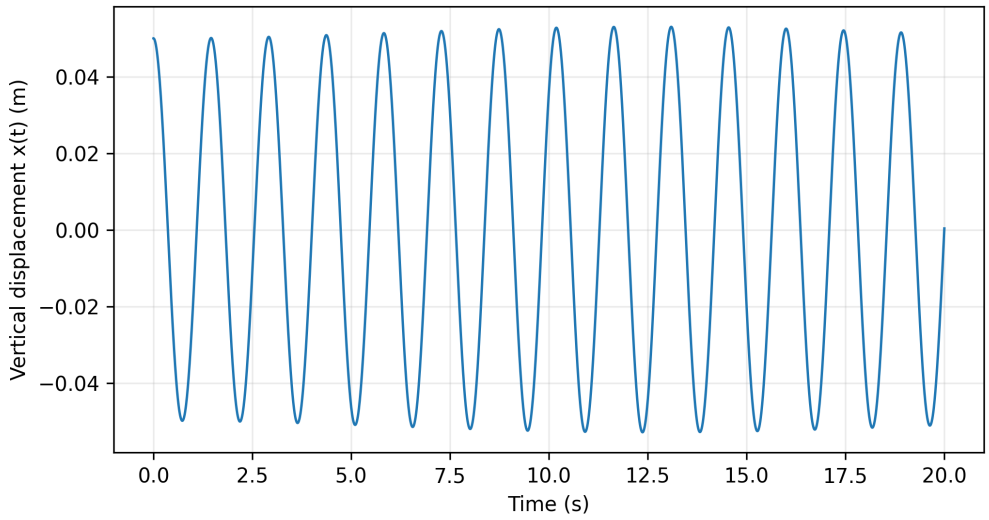

Figure 2. Numerical vertical response $x(t)$ for the baseline parameter set.

The engine swing angle is shown in Figure 3. Starting from 5°, the angle oscillates between approximately −5° and 5°. The angular response has a lower dominant frequency than the vertical spring response, which is consistent with the two natural frequencies obtained from the local linear approximation. Since the vertical coordinate is positive upward, negative values of $x(t)$ indicate that the wing support moves below its static equilibrium position. Similarly, negative values of $\theta(t)$ indicate motion opposite to the defined positive angular direction.

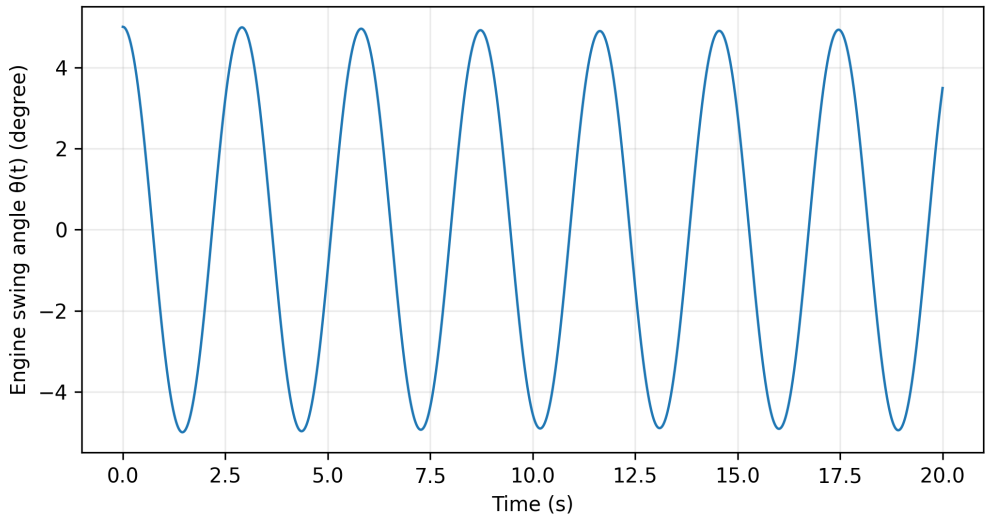

Figure 3. Numerical engine swing angle $\theta(t)$ for the baseline parameter set.

4.3. Effect of spring stiffness

The baseline spring stiffness is set to $k_0 = 20{,}000$ N/m. To investigate the sensitivity of the system response to changes in spring stiffness, two additional values, namely 15,000 and 25,000 N/m, are considered. These values represent a symmetric variation of −25% and +25%, respectively, from the baseline stiffness. Thus, the three stiffness values provide a consistent basis for examining the

influence of stiffness below, at, and above the reference configuration. For each case, all other model parameters and initial conditions are kept unchanged, and the simulations are conducted over the time interval $0 \le t \le 10$ s. According to the linear natural-frequency relationship $f_y^{\mathrm{lin}} = \frac{1}{2\pi}\sqrt{\frac{k}{m}}$, the selected stiffness values correspond to vertical natural frequencies of approximately 0.616, 0.712, and 0.796 Hz, respectively. Figure 4 compares the resulting vertical responses, illustrating how changes in spring stiffness affect the oscillatory behavior of the nonlinear system.

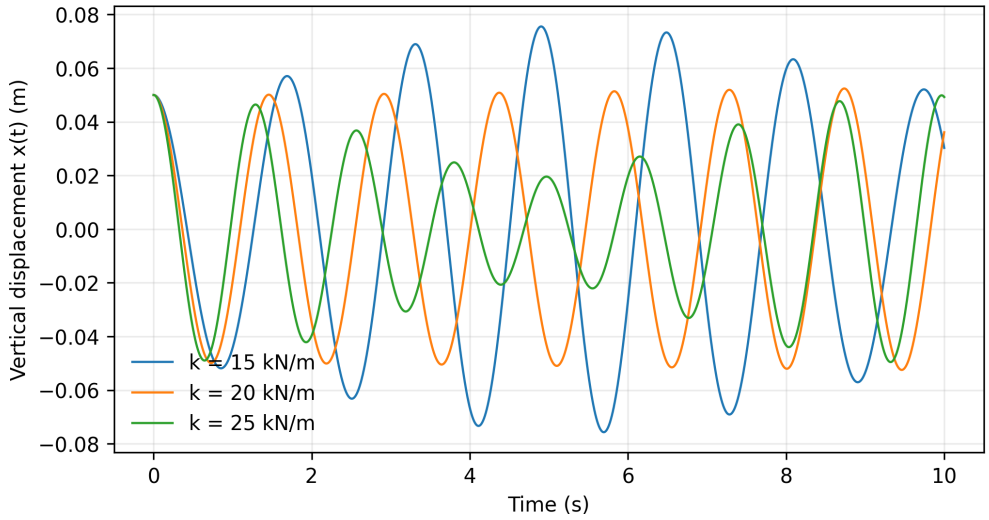

Figure 4. Comparison of the vertical response for three spring-stiffness values.

Since the positive vertical direction is upward and $x(t)$ is measured relative to the static equilibrium position, negative values in Figure 4 indicate downward displacements of the wing support relative to its corresponding equilibrium position. The maximum absolute vertical and angular responses over a prescribed simulation interval $0 \le t \le T$ are defined as

$$x_{\max}(T) = \max_{0\le t\le T} |x(t)|, \qquad \theta_{\max}(T) = \max_{0\le t\le T} |\theta(t)|.$$

For the spring-stiffness comparison, the maximum responses are evaluated over $T = 10$ s. The numerical results for the three spring-stiffness values are summarized in Table 3, with the angular response values converted from radians to degrees for presentation.

Table 3. Numerical response for variation of spring stiffness.

k (N/m)	f_y^{lin} (Hz)	$\max\|x(t)\|$ (m)	$\max\|\theta(t)\|$ (degree)
15,000	0.616	0.0757	5.000
20,000	0.712	0.0525	5.000
25,000	0.796	0.0500	5.795

For the selected initial-value problem, the maximum absolute vertical displacement decreases from approximately 0.0757 m at $k = 15{,}000$ N/m to 0.0500 m at $k = 25{,}000$ N/m. This result should be interpreted only for the selected parameter values, initial conditions, and simulation interval because the system is nonlinear.

It is also noteworthy that the maximum absolute angular response for $k = 25{,}000$ N/m reaches approximately 5.795°, exceeding the initial angular displacement of 5°. This maximum corresponds to

a negative angular displacement of approximately -5.795° at $t = 4.298$ s. In contrast, for $k = 15{,}000$ and 20,000 N/m, the maximum absolute angular response over the same interval remains at its initial value of 5°. This difference illustrates the influence of nonlinear interaction between the vertical and angular motions under the selected parameter conditions. It should not be interpreted as a general relationship between spring stiffness and angular response.

To further examine the consistency between the analytical natural frequencies and the numerical responses, a comparison was performed for the three spring-stiffness values. For this purpose, additional simulations were conducted over the interval $0 \le t \le 20$ s using the same solver settings, parameter values, and initial conditions.

The numerical frequencies were estimated from the time intervals between successive positive local maxima of the vertical displacement and angular response. Let $t_{y,j}$ and $t_{\theta,j}$ denote the times at which the j-th positive local maxima of $x(t)$ and $\theta(t)$ occur, respectively. The corresponding numerical frequencies are calculated as

$$f_y^{\text{num}} = \left[\frac{1}{N_y - 1} \sum_{j=1}^{N_y - 1} (t_{y,j+1} - t_{y,j}) \right]^{-1},$$

$$f_\theta^{\text{num}} = \left[\frac{1}{N_\theta - 1} \sum_{j=1}^{N_\theta - 1} (t_{\theta,j+1} - t_{\theta,j}) \right]^{-1},$$

where N_y and N_θ denote the numbers of detected positive local maxima of the vertical displacement and angular response, respectively. The relative errors between the analytical and numerical frequencies are calculated as

$$\varepsilon_f = \frac{|f^{\text{num}} - f^{\text{lin}}|}{f^{\text{lin}}} \times 100\%.$$

Table 4. Comparison of analytical and numerically estimated oscillation frequencies.

k (N/m)	Mode	f^{lin} (Hz)	f^{num} (Hz)	ε_f (%)
15,000	Vertical	0.6164	0.6175	0.18
	Angular	0.3525	0.3547	0.63
20,000	Vertical	0.7118	0.6878	3.37
	Angular	0.3525	0.3435	2.55
25,000	Vertical	0.7958	0.8045	1.10
	Angular	0.3525	0.3524	0.01

The comparison shows that the numerically estimated frequencies are generally close to the analytical predictions, although differences are observed among the parameter cases. The largest relative error occurs in the vertical response for $k = 20{,}000$ N/m, amounting to approximately 3.37%. For the angular response at the same spring stiffness, the relative error is approximately 2.55%. These differences are associated with the nonlinear characteristics of the governing equations, which are not represented in the first-order linear approximation. Therefore, the analytical natural frequencies describe the local small-oscillation behavior, whereas the numerical frequencies characterize the oscillatory responses under the specified initial conditions and simulation interval.

4.4. Energy Conservation and Numerical Sensitivity

Since the proposed model neglects damping and external forcing, the mechanical energy of the system should remain constant along its trajectories. In the shifted coordinate, the mechanical energy relative to its value at equilibrium is given by

$$E_r(t) = \frac{1}{2}m\left(\dot{x}^2 + L^2\dot{\theta}^2 + 2L\dot{x}\dot{\theta}\sin\theta\right) + \frac{1}{2}kx^2 + mgL(1-\cos\theta).$$

The numerical conservation of energy was assessed using the maximum relative energy deviation over the 20-s simulation interval, defined as

$$\delta_E = \max_{0\le t\le 20}\frac{|E_r(t) - E_r(0)|}{E_r(0)}.$$

For the baseline solver settings (rtol = 10^{-10}, atol = 10^{-12}, and a maximum step size of 0.01 s), the maximum relative energy deviations for k = 15,000, 20,000, and 25,000 N/m were 1.90×10^{-14}, 1.45×10^{-14}, and 1.60×10^{-14}, respectively. These values indicate that the numerical solutions preserve the mechanical energy to within a small numerical error over the simulated interval.

A numerical sensitivity test was also conducted by repeating the simulations for all three spring-stiffness values using two alternative sets of solver settings. In addition to the baseline settings, a looser configuration with rtol = 10^{-8}, atol = 10^{-10}, and a maximum step size of 0.05 s, and a tighter configuration with rtol = 10^{-12}, atol = 10^{-14}, and a maximum step size of 0.005 s were considered. The output interval was kept at 0.001 s in all cases. The simulations were compared over both the 10-s interval used for the stiffness-response analysis and the 20-s interval used for the baseline responses and frequency estimation.

Relative to the baseline computation, the maximum relative change in the maximum displacement and angular responses did not exceed $9.05\times10^{-10}\%$ for the looser settings and $4.52\times10^{-13}\%$ for the tighter settings. The numerically estimated frequencies were unchanged to four decimal places. The maximum relative energy deviations under the looser and tighter settings were 1.24×10^{-11} and 1.93×10^{-14}, respectively. These comparisons indicate that the reported numerical responses are insensitive to the tested solver tolerances and maximum step sizes for the parameter values and time intervals considered.

5. Discussion

The model provides a direct mathematical connection between the vertical motion of the wing support and the angular motion of the engine. In the original formulation, $\ddot{y}$ appears in the pendulum equation and $\ddot{\theta}$ appears in the vertical equation. After eliminating these accelerations, the nonlinear coupling can be examined more explicitly through Equations (13) and (14). The vertical acceleration depends on the angular velocity and displacement through terms involving $\dot{\theta}^2$ and $\sin^2\theta$, whereas the angular acceleration depends on the vertical displacement through the term involving $(kx/m - g)\tan\theta$. These terms indicate that the vertical and angular motions are dynamically interdependent. This behavior is consistent with the characteristics of coupled nonlinear oscillatory systems, in which interactions between generalized coordinates may influence the overall vibration response [20, 28]. However, the presence of nonlinear coupling does not by itself establish significant energy transfer between the two motions, which would require a separate quantitative analysis of the energy associated with each coordinate.

The local linearization gives two natural frequencies, one determined by the spring-to-mass ratio k/m and the other by the gravity-to-length ratio g/L, as expressed in Equation (16). At first order, the two modes are uncoupled, whereas the coupling remains present through the nonlinear terms in the original equations. This occurs because terms such as $\dot{\theta}^2$, $\sin^2\theta$, and $x\tan\theta$ are of second or higher order and therefore do not contribute to the first-order approximation in Equation (15). Consequently, the uncoupled modes obtained from linearization do not imply that the original nonlinear system is

dynamically independent. The comparison between analytical and numerically estimated frequencies in Table 4 shows that the numerical frequencies are generally close to the analytical predictions, although some differences are observed. The largest relative differences occur for the baseline spring stiffness of 20,000 N/m, amounting to approximately 3.37% for the vertical response and 2.55% for the angular response. These differences reflect the nonlinear characteristics of the governing equations and the finite-interval estimation of oscillation frequencies from the numerical responses. Thus, the analytical frequencies represent local small-oscillation predictions, whereas the numerical frequencies characterize the mean oscillation rates under the specified initial conditions and simulation interval.

The stiffness comparison also shows that changes in the equivalent wing stiffness affect both the frequency and magnitude of the vertical response. As expected from the analytical relationship $f_y^{\text{lin}} = (1/2\pi)\sqrt{k/m}$, increasing the spring stiffness raises the vertical natural frequency. For the selected initial conditions and the 10-s simulation interval, the maximum absolute vertical displacement decreases from approximately 0.0757 m at $k = 15{,}000$ N/m to 0.0500 m at $k = 25{,}000$ N/m, as summarized in Table 3. This trend should not be interpreted as a general inverse relationship between spring stiffness and maximum displacement, since the response of the nonlinear system also depends on the initial conditions and the selected simulation interval. The angular response further illustrates this dependence. For $k = 25{,}000$ N/m, the maximum absolute angular displacement reaches approximately $5.795°$, exceeding the initial angular displacement of $5°$. This value corresponds to a negative angular displacement of approximately $-5.795°$ at $t = 4.298$ s. In contrast, for $k = 15{,}000$ and 20,000 N/m, the maximum absolute angular response over the same interval remains at its initial value of $5°$. These results indicate that the effects of spring stiffness on vertical and angular responses are not necessarily identical. Such behavior should be interpreted specifically for the parameter values, initial conditions, and simulation interval considered in this study.

The proposed model is related to previous studies on coupled pendulum and vibration-absorber systems, but differs in its mechanical configuration and analytical objectives. Amer et al. [20] investigated the motion of a pendulum attached to a tuned absorber near resonance conditions, while Amer et al. [23] examined a two-degree-of-freedom dynamical tuned-absorber system operating close to resonance. More recently, Zhang et al. [24] investigated large-amplitude vibrations and nonlinear dynamics in an autoparametric pendulum absorber-harvester system. These studies share an interest in nonlinear interactions involving pendulum motion and coupled mechanical degrees of freedom. Related investigations have also addressed energy exchange in pendulum–absorber systems [21], experimental validation of pendulum-based nonlinear absorbers [22], and vibration mitigation using nonlinear energy sinks under different excitation conditions [29, 30]. Recent work on pendulum absorbers attached to elastic structures further illustrates the range of configurations considered in nonlinear vibration research [31–33]. However, their configurations and research objectives differ from those considered here. The present study focuses on representing the vertical flexibility of a wing support and the angular motion of an underwing engine within a simplified spring–pendulum framework. Yaman and Dalmış [1] investigated the influence of under-wing store mass on the flutter response of an F-16 model wing through wind-tunnel experiments and numerical analysis. Their results showed that increasing store mass reduces the flutter frequency and flutter speed. Recent studies have also examined engine-induced vibration loads at the pylon–wing interface [2] and nonlinear aeroelastic models of flexible wings [7], while reviews have summarized advances in wing and panel aeroelasticity [4, 5]. Compared with such structural representations, the present model adopts a more reduced mechanical configuration by representing the wing flexibility as an equivalent linear spring and the engine as a point mass connected through a rigid support. Therefore, its contribution lies in the mathematical formulation and analysis of this particular reduced-order configuration, rather than in reproducing the detailed structural or aeroelastic behavior of an actual aircraft.

The numerical energy assessment further supports the consistency of the computational results. Because the model excludes damping and external forcing, its total mechanical energy is theoretically conserved. The maximum relative energy deviations obtained from the baseline numerical simulations do not exceed approximately 1.90×10^{-14} over the 20-s interval for the three spring-stiffness values considered. In addition, the numerical sensitivity tests show that changes in the solver tolerances and maximum integration step size produce negligible differences in the calculated maximum responses and estimated frequencies. The maximum relative changes in the response extrema remain below $9.05 \times 10^{-10}\%$ for the looser solver settings and $4.52 \times 10^{-13}\%$ for the tighter settings. The numerically estimated frequencies also remain unchanged to four decimal places. These results indicate that the numerical responses are insensitive to the tested computational settings for the parameter values and simulation intervals considered. Nevertheless, conservation of the total mechanical energy does not, by itself, quantify the transfer of energy between the vertical and angular motions.

The present model is intentionally simplified and does not include aerodynamic forces, pylon bending deformation, distributed wing mass, external excitation due to turbulence or landing impacts, or structural damping. Therefore, the model should not be used to predict actual aircraft loads or to claim that the oscillations will decay with time. Similarly, the bounded responses observed in the numerical simulations should be interpreted only over the specified simulation intervals and should not be regarded as a general conclusion regarding the global behavior of the nonlinear system. Its main value is as a tractable low-order mathematical model for examining the interaction between vertical elastic motion and angular pendulum motion. Further investigations may incorporate more detailed structural properties, damping mechanisms, and external excitation to obtain a more comprehensive representation of wing–engine dynamics.

6. Conclusions

A coupled spring–pendulum model has been developed to represent the vertical oscillation of an aircraft wing support and the angular motion of an underwing engine. Using the Lagrangian formulation, two coupled nonlinear second-order differential equations are obtained for the vertical displacement and angular motion. The system has an equilibrium configuration at $(y^*, \theta^*) = (-mg/k, 0)$, which becomes $(x^*, \theta^*) = (0, 0)$ after shifting the vertical coordinate. The local linearization around this equilibrium yields two independent harmonic oscillators with natural angular frequencies $\omega_y = \sqrt{k/m}$ and $\omega_\theta = \sqrt{g/L}$. The corresponding eigenvalues are purely imaginary, indicating neutral stability of the linearized undamped system rather than asymptotic stability.

Numerical simulations demonstrate that the vertical and angular responses remain bounded over the specified simulation intervals. The stiffness investigation shows that increasing the spring stiffness raises the vertical natural frequency and changes the maximum vertical displacement under the selected initial conditions. In particular, the maximum absolute angular response reaches approximately 5.795° for $k = 25{,}000$ N/m over the 10-s simulation interval. Furthermore, the comparison between analytical and numerically estimated frequencies shows generally close agreement, with relative errors not exceeding approximately 3.37% for the parameter cases considered. The numerical energy assessment and sensitivity tests also indicate good conservation of mechanical energy and consistency of the numerical results under the tested solver settings. Since the model neglects aerodynamic effects, structural damping, and external excitation, its results should be interpreted as those of an idealized mechanical representation rather than predictions of actual aircraft behavior. Further work may incorporate more detailed structural properties, damping mechanisms, and external excitation to obtain a more comprehensive representation of wing–engine dynamics.

Acknowledgement

The authors thank the Department of Civil Engineering, Jenderal Soedirman University, for academic support during the preparation of this article.

REFERENCES

[1] K. Yaman and M. B. Dalmış, "Influence of under-wing store mass on the flutter response of an f-16 model wing," *Transactions of FAMENA*, vol. 50, no. 2, pp. 21–38, 2026. https://doi.org/10.21278/TOF.502080725.

[2] S. F. Zettel, M. Böswald, R. D. Dewald, and R. Winter, "Jet engine vibration model for estimating pylon–wing interface loads for realistic structural excitation," *CEAS Aeronautical Journal*, vol. 17, pp. 1381–1394, 2026. First published online 10 December 2025. https://doi.org/10.1007/s13272-025-00931-1.

[3] R. N. Al-Dala'ien, J. E. AlQasimi, M. J. Al-Ezzi, A. Al-Shehri, N. A. A. Qasem, S. M. Ghazzawi, and A. Baluch, "Evolution of tuned mass dampers: From structural vibration control to aeroelastic applications in flexible aircraft wings: A review," *Journal of Vibration Engineering & Technologies*, vol. 14, p. 444, 2026. https://doi.org/10.1007/s42417-026-02649-8.

[4] Y. Chai, W. Gao, B. Ankay, F. Li, and C. Zhang, "Aeroelastic analysis and flutter control of wings and panels: A review," *International Journal of Mechanical System Dynamics*, vol. 1, no. 1, pp. 5–34, 2021. https://doi.org/10.1002/msd2.12015.

[5] M. Berci, "On aerodynamic models for flutter analysis: A systematic overview and comparative assessment," *Applied Mechanics*, vol. 2, no. 3, pp. 516–541, 2021. https://doi.org/10.3390/applmech2030029.

[6] Q. Liu, Y. Xu, J. Kurths, and X. Liu, "Complex nonlinear dynamics and vibration suppression of conceptual airfoil models: A state-of-the-art overview," *Chaos*, vol. 32, no. 6, p. 062101, 2022. https://doi.org/10.1063/5.0093478.

[7] S. Jayatilake, M. Lowenberg, B. K. S. Woods, and B. Titurus, "Nonlinear aeroelastic modelling and analysis of a geometrically nonlinear wing with combined unsteady sectional and lifting line aerodynamics," *Nonlinear Dynamics*, vol. 113, no. 12, pp. 14657–14693, 2025. https://doi.org/10.1007/s11071-025-10936-4.

[8] Y. Yang, J. Zhang, and P. Xia, "Dynamic stability analysis of rotor–nacelle–wing coupling system with stochasticity and freeplay nonlinearity," *Aerospace Science and Technology*, vol. 177, p. 112735, 2026. https://doi.org/10.1016/j.ast.2026.112735.

[9] M. Kong, B. Pei, Q. Liu, and Y. Xu, "Dynamics and reliability design of rotor–nacelle–wing coupled structures under non-white random gusts," *Aerospace Science and Technology*, vol. 171, p. 111659, 2026. https://doi.org/10.1016/j.ast.2026.111659.

[10] M. Abramovitz, "Experimental investigation of elastic mode control on a model of a transport aircraft," tech. rep., NASA Technical Reports Server, 1981. NASA document 19840019653, https://ntrs.nasa.gov/citations/19840019653.

[11] S. S. Rao, *Mechanical Vibrations*. Pearson, 6 ed., 2017. https://www.pearson.com/en-us/subject-catalog/p/mechanical-vibrations/P200000003352.

[12] C. An, D. Zhang, R. Zhao, C. Xie, and C. Yang, "Structural reduced-order model including geometrical nonlinearities and application to aeroelastic behavior analysis," *Aerospace Science and Technology*, vol. 168, p. 111209, 2026. https://doi.org/10.1016/j.ast.2025.111209.

[13] M. Candon, E. Hale, M. Balajewicz, A. Delgado-Gutiérrez, V. Muscarello, *et al.*, "Parameterization of nonlinear aeroelastic reduced order models via direct interpolation of taylor partial

derivatives," *Nonlinear Dynamics*, vol. 112, pp. 17649–17670, 2024. https://doi.org/10.1007/s11071-024-09976-z.

[14] H. Goldstein, C. Poole, and J. Safko, *Classical Mechanics*. Addison-Wesley, 3 ed., 2002. https://physicsgg.me/wp-content/uploads/2014/12/classical_mechanics_goldstein_3ed.pdf.

[15] J. H. Ginsberg, M. S. Allen, and P. A. Voglewede, *Engineering Dynamics*. Cambridge University Press, 2 ed., 2026. https://doi.org/10.1017/9781009711685.

[16] J. R. Mohallem, *Lagrangian and Hamiltonian Mechanics: A Modern Approach with Core Principles and Underlying Topics*. Cham: Springer, 2024. https://doi.org/10.1007/978-3-031-55202-1.

[17] V. Moretti, *Analytical Mechanics: Classical, Lagrangian and Hamiltonian Mechanics, Stability Theory, Special Relativity*. Cham: Springer, 2023. https://doi.org/10.1007/978-3-031-27612-5.

[18] K. Kecik, "Assessment of energy harvesting and vibration mitigation of a pendulum dynamic absorber," *Mechanical Systems and Signal Processing*, vol. 106, pp. 198–209, 2018. https://doi.org/10.1016/j.ymssp.2017.12.028.

[19] H. F. Abundis-Fong, J. Enríquez-Zárate, A. Cabrera-Amado, and G. Silva-Navarro, "Optimum design of a nonlinear vibration absorber coupled to a resonant oscillator: A case study," *Shock and Vibration*, vol. 2018, p. 2107607, 2018. Article ID 2107607. https://doi.org/10.1155/2018/2107607.

[20] W. S. Amer, M. A. Bek, and M. K. Abohamer, "On the motion of a pendulum attached with tuned absorber near resonances," *Results in Physics*, vol. 11, pp. 291–301, 2018. https://doi.org/10.1016/j.rinp.2018.09.005.

[21] G. Hurel, A. T. Savadkoohi, and C.-H. Lamarque, "Nonlinear vibratory energy exchanges between a two-degree-of-freedom pendulum and a nonlinear absorber," *Journal of Engineering Mechanics*, vol. 145, no. 8, 2019. https://doi.org/10.1061/(ASCE)EM.1943-7889.0001620.

[22] G. Hurel, "Design of a nonlinear absorber for a 2 degrees of freedom pendulum and experimental validation," *Structural Control and Health Monitoring*, vol. 28, no. 11, p. e2814, 2021. https://doi.org/10.1002/stc.2814.

[23] T. S. Amer, S. A. Abdelhfeez, and R. F. Elbaz, "Modeling and analyzing the motion of a 2dof dynamical tuned absorber system close to resonance," *Archive of Applied Mechanics*, vol. 93, pp. 785–812, 2023. https://doi.org/10.1007/s00419-022-02299-8.

[24] A. Zhang, Z. Gao, H. Li, P. Han, Z. Song, and W. Yu, "Large amplitude vibrations and nonlinear dynamics characteristics of an autoparametric pendulum absorber-harvester," *International Journal of Non-Linear Mechanics*, vol. 178, p. 105201, 2025. https://doi.org/10.1016/j.ijnonlinmec.2025.105201.

[25] P. Virtanen, R. Gommers, T. E. Oliphant, M. Haberland, T. Reddy, D. Cournapeau, E. Burovski, P. Peterson, W. Weckesser, J. Bright, S. J. van der Walt, M. Brett, J. Wilson, K. J. Millman, N. Mayorov, A. R. J. Nelson, E. Jones, R. Kern, E. Larson, C. J. Carey, I. Polat, Y. Feng, E. W. Moore, J. VanderPlas, D. Laxalde, J. Perktold, R. Cimrman, I. Henriksen, E. A. Quintero, C. R. Harris, A. M. Archibald, A. H. Ribeiro, F. Pedregosa, P. van Mulbregt, and SciPy 1.0 Contributors, "Scipy 1.0: Fundamental algorithms for scientific computing in python," *Nature Methods*, vol. 17, pp. 261–272, 2020. https://doi.org/10.1038/s41592-019-0686-2.

[26] E. Hairer, S. P. Norsett, and G. Wanner, *Solving Ordinary Differential Equations I: Nonstiff Problems*. Springer, 2 ed., 1993. https://doi.org/10.1007/978-3-540-78862-1.

[27] National Institute of Standards and Technology, "CODATA Value: Standard Acceleration of Gravity." The NIST Reference on Constants, Units, and Uncertainty, 2022. https://physics.nist.gov/cgi-bin/cuu/Value?gn.

[28] A. H. Nayfeh and D. T. Mook, *Nonlinear Oscillations*. John Wiley & Sons, 1979. https://doi.org/10.1002/9783527617586.

[29] J. Chen, W. Zhang, J. Liu, *et al.*, "Vibration absorption of parallel-coupled nonlinear energy sink under shock and harmonic excitations," *Applied Mathematics and Mechanics (English Edition)*, vol. 42, pp. 1135–1154, 2021. https://doi.org/10.1007/s10483-021-2757-6.

[30] A. S. Saeed, R. A. Nasar, and M. A. AL-Shudeifat, "A review on nonlinear energy sinks: Designs, analysis and applications of impact and rotary types," *Nonlinear Dynamics*, vol. 111, pp. 1–37, 2023. https://doi.org/10.1007/s11071-022-08094-y.

[31] J. Pan, V. Sorokin, L. Tang, A. Hall, and A. Zhang, "Elastic wave transmission and reflection in a rod with an attached nonlinear autoparametric pendulum absorber," *Journal of Sound and Vibration*, vol. 619, p. 119404, 2025. Article 119404. https://doi.org/10.1016/j.jsv.2025.119404.

[32] Q. Cai and S. Zhu, "Nonlinear double-mass pendulum for vibration-based energy harvesting," *Nonlinear Dynamics*, vol. 112, pp. 5109–5128, 2024. https://doi.org/10.1007/s11071-023-09236-6.

[33] M. Sun, J. Chen, T. Quan, *et al.*, "Enhancements of vibration absorption of nonlinear energy sink by additional degree of freedom oscillator," *Journal of Nonlinear Mathematical Physics*, vol. 33, p. 38, 2026. Article 38. https://doi.org/10.1007/s44198-026-00386-w.